

A CFH12k Lensing Survey of X-ray Luminous Galaxy Clusters

I: Weak Lensing Methodology

S. Bardeau¹, J.-P. Kneib^{1,2}, O. Czoske^{3,1}, G. Soucail¹, I. Smail⁴, and H. Ebeling⁵

¹ Observatoire Midi-Pyrénées, UMR5572, 14 Avenue Edouard Belin, 31400 Toulouse, France.

² Caltech, Astronomy, 105-24, Pasadena, CA 91125, USA.

³ Institut für Astrophysik und Extraterrestrische Forschung, Auf dem Hügel 71, 53121 Bonn, Germany.

⁴ Institute for Computational Cosmology, University of Durham, South Road, Durham DH1 3LE, UK.

⁵ Institute for Astronomy, University of Hawaii, 2680 Woodlawn Dr, Honolulu, HI 96822, USA

Received sometime; accepted later

Abstract. We present the weak lensing methodology applied to our multi-colour imaging survey of X-ray luminous galaxy clusters conducted with the wide field CFH12k camera. This method, which is converting a fully reduced CFH12k image into cluster mass constraints, is done in two steps that we explain in detail: (1) determination of the "true" shape of faint (lensed) galaxies which involves: object detection strategy, point spread function (PSF) determination, galaxy shapes measurements with errors; (2) conversion of the faint galaxies catalogue into useful mass constraints which is done by different lensing techniques using 1D and/or 2D mass estimates. Finally, we compare the cluster mass model to the light distribution of cluster members as observed on our imaging data. To illustrate the method, we apply it to the well studied cluster Abell 1689 ($z = 0.184$). In this cluster, we detect the gravitational shear signal to the edge of the image at 3σ significance. The two-dimensional mass reconstruction has a $\sim 10\sigma$ significance mass peak centered on the brightest cluster galaxy. The weak lensing constraints are well fitted by a NFW mass profile with $M_{200} = 14.1^{+6.3}_{-4.7} \times 10^{14} M_{\odot}$, and $c = 3.5^{+0.5}_{-0.3}$ ($\chi^2 = 0.33$), or by a power law (PL) profile with $q = 0.75 \pm 0.07$ and $\theta_E = 14''.6 \pm 0''.3$ ($\chi^2 = 0.64$). The mass-to-light ratio is found to be almost constant with radius with a mean value of $M/L_R = 150 h (M/L)_{\odot}$. We compare these results to other weak lensing analyses of Abell 1689 presented in the literature and find good agreements in terms of the shear measurement as well as the final mass estimate.

Key words. Gravitational lensing: weak lensing – Galaxies: clusters – Clusters of Galaxies: individual (Abell 1689)

1. Introduction

Clusters of galaxies are the most massive collapsed structures located at the nodes of the filamentary web structure of the Universe (e.g. the mapping of SDSS and 2dF). These massive systems are the focus of both theoretical (e. g. Eke et al. 1996; Bahcall et al. 1997; Viana & Liddle 1998) and observational studies. The aim is to better understand cluster formation and evolution and thus it is important to quantify their physical properties (mass distribution, mass density profile, importance of substructure, etc.). Different techniques such as galaxy dynamics, X-rays, Sunyaev-Zeldovich effect or gravitational lensing, are available to probe the physical properties of clusters. Gravitational lensing is a particularly attractive method as it is directly sensitive to the total mass distribution irrespective of its physical state (see the review by Mellier 1999).

Although the study of a single cluster can be instructive, we need to study homogeneous samples of massive clusters in order to better understand cluster physics, test theoretical predictions and to constrain the cosmological and physical param-

eters governing the growth of structure in the Universe. Indeed, clusters are expected to show some variation in their properties, in particular regarding the amount of substructure and their merger history which can be directly probed by measuring their mass distribution.

In order to obtain a better understanding of cluster mass distributions from small to large scale, we have selected a sample of X-ray luminous clusters (Czoske et al. 2003; Smith et al. 2004) identified in the XBACs sample (X-ray Brightest Abell-type Clusters: Ebeling et al. 1996). All these clusters have an X-ray luminosity $L_X \geq 8 \times 10^{44} \text{ erg s}^{-1}$ in the range 0.1–2.4 keV band, and are all in a narrow redshift slice at $z \sim 0.2$ (from $z_{A2218} = 0.171$ to $z_{A1835} = 0.253$). As XBACS is restricted to Abell clusters (Abell et al. 1989), it is X-ray flux limited but not truly X-ray selected. However, a comparison with the X-ray selected *ROSAT* Brightest Cluster Sample (BCS: Ebeling et al. 1998, 2000) shows that $\sim 75\%$ of the BCS clusters in the redshift and X-ray luminosity range of our sample are in fact Abell clusters. Hence, our XBACs sample is, in all practical aspects, indistinguishable from an X-ray selected sample.

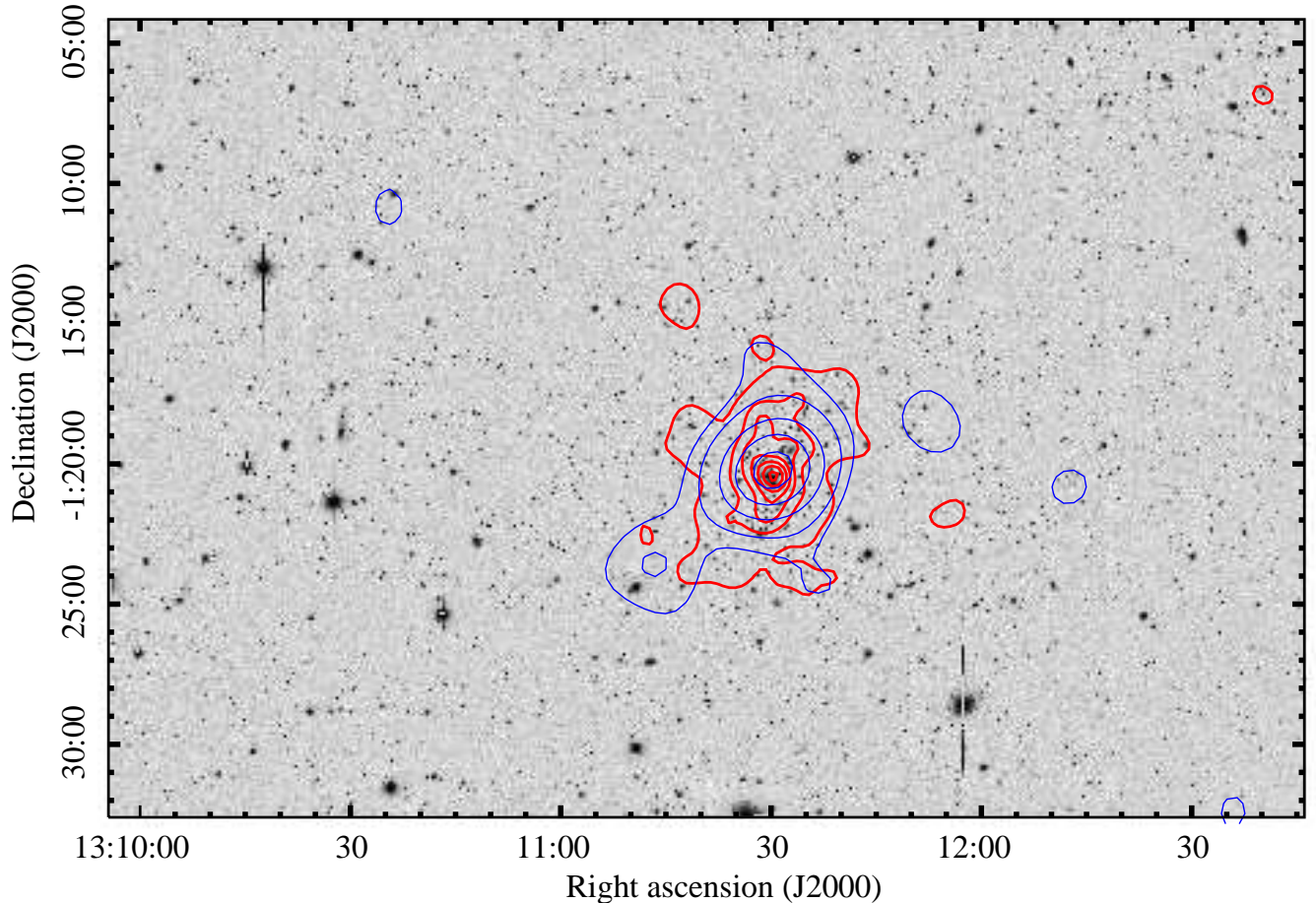


Fig. 1. The full $42' \times 28'$ CFH12k R-band image of Abell 1689. The thick contours represent the number density of bright galaxies selected in the R-band: the first level corresponds to 5 objects per square arcmin, increased by steps of 5 units. The maximal density is $36.5 \text{ galaxies arcmin}^{-2}$ in the cluster center. The thin contours represent the mass density reconstruction with LENSENT2 and an ICF of $180''$ (see Sect. 4.2 for more details). Contour levels are respectively 2, 3, 5, 7 and 9σ , while the peak value corresponds to a mass density of $1100 h_{70} M_{\odot} \text{pc}^{-2}$. North is to the top, East to the right.

Using the CFH12k wide field camera (Cuillandre et al. 2000) mounted at the Canada-France-Hawaii Telescope (CFHT), we imaged 11 clusters of the above sample in the B, R and I bands. In the present paper we present the *weak lensing methodology* applied to our cluster sample.

The first step of any weak lensing work is to correct the observed galaxy ellipticities from any observational smearing: circularisation effect and anisotropy of the point spread function (PSF). The classical approach to do this is the so-called KSB method (Kaiser et al. 1995), implemented in the *IMCAT* software (see also Luppino & Kaiser 1997; Rhodes et al. 2000; Kaiser 2000). The basic idea is to relate the “true” ellipticity of the background sources to the observed ellipticity through polarizability tensors, which include the smearing effect of the PSF, possibly with anisotropic components. In practice these can be computed through the combination of the second order moments of the light distribution of the galaxies and the PSF itself. Contrary to this *direct* approach, we will use in this paper an *inverse* approach through a maximum likelihood or bayesian estimate of the source galaxy shape convolved by the local PSF (this method was first proposed by Kuijken 1999). Both the

galaxy shape and the local PSF are modelled in terms of sums of elliptical Gaussians. This approach is implemented in the software *Im2SHAPE* which has been developed by Bridle et al. (2001). The main advantage of *Im2SHAPE* is that it gives direct estimates of the uncertainties of the recovered parameters of the sources and these uncertainties can then be included in the mass inversion.

In the weak lensing limit, the ellipticities of background galaxies give an unbiased estimate of the shear field induced by the gravitational potential of the foreground cluster. The estimate is inherently noisy due to the shape measurements errors and the intrinsic ellipticities of the galaxies. Several methods have been proposed to reconstruct the mass density field (or the potential) of the foreground structure from the measured shear field. Non-parametric methods are usually best to produce a mass-map, allowing to identify mass peaks. They can also be used to estimate the cluster mass profile by means of the aperture mass densitometry method (Fahlman et al. 1994; Schneider 1996). On the other hand parametric methods are best to constrain the cluster mass profile and total mass by fitting a radial shear profile to the galaxy ellipticities.

To illustrate the various methods and techniques used, we apply our procedure to the well studied cluster Abell 1689. Abell 1689 at redshift $z = 0.184$ is part of our cluster sample and is also one of the richest clusters ($R = 4$) in the Abell catalog. The central structure of this cluster is complex: from the redshift distribution of 66 cluster members Girardi et al. (1997) find evidence for a superposition of several groups along the line of sight to the cluster centre which explains the extraordinarily high velocity dispersion of $2355^{+238}_{-183} \text{ km s}^{-1}$. Czoske (2004) has recently obtained a new large dataset of more than 500 cluster galaxy redshifts in this cluster, which will help elucidate the galaxy distribution Abell 1689. Preliminary analysis of these data shows that the large scale distribution of galaxies in and around Abell 1689 is in fact rather smooth and that significant substructure seems confined to the very centre of the cluster. It therefore makes sense to model the large-scale mass distribution of the cluster with simple models, such as the “universal” mass profile proposed by Navarro et al. (1997) (NFW).

Abell 1689 is a powerful cluster lens and has been studied by various groups using different lensing techniques (Tyson et al. 1990; Tyson & Fischer 1995; Taylor et al. 1998; Clowe & Schneider 2001; King et al. 2002). It has also been studied in X-rays using *Chandra* (Xue & Wu 2002) and *XMM-Newton* (Andersson & Madejski 2004).

This paper is organised as follows: Sect. 2 briefly presents the observations of Abell 1689 used in this paper and gives a summary of the data reduction procedure and the conversion of the reduced data into catalogues that are useful for the weak lensing analysis. In Sect. 3 we present the measurement of galaxy shapes and correction for PSF anisotropy using Im2SHAPE. In Sect. 4 we convert the galaxy shape measurements into two-dimensional shear maps and radial shear profiles. Sect. 5 explains how we model the lensing data using both 1D and 2D techniques. In Sect. 6 we compare the lensing mass to the light distribution. Finally in Sect. 7 we discuss our method and results. In a separate paper (Bardeau et al. 2004, in prep.) we will present a thorough mass distribution analysis of A1689 combining the weak and strong lensing mass measurements.

We assume $H_0 = 70 \text{ km s}^{-1} \text{ Mpc}^{-1}$, $\Omega_m = 0.3$, $\Omega_\Lambda = 0.7$. At the redshift of the cluster Abell 1689 ($z = 0.1840$), $1''$ corresponds to 3.09 kpc (and $1'$ to 185 kpc).

2. Observations and Cataloguing

We observed Abell 1689 with the CFH12k camera through the B, R and I filters (Fig. 1 shows the R-band image) between 30 May and 2 June 2000. The camera consists of 12 CCD chips of $2k \times 4k$ pixels with a total field of view of $42' \times 28'$ at a pixel scale of $0''.205$. The log of the observations of Abell 1689 ($\alpha_{J2000} = 13^h 11^m 30^s$, $\delta_{J2000} = -01^\circ 20' 28''$) is summarised in the first part of Table 1.

2.1. Data reduction

For a detailed description of the data reduction see (Czoske 2002). Here we just give a brief outline. Prereduction of the

CFH12k data was done in a standard way using the IRAF¹ package *mscred* (Valdes 1998) for bias subtraction and flat-fielding using twilight sky images.

Fringing in the *I* band images was removed by subtracting a correction image constructed from eight science images from different fields taken during the same night after masking any objects detected in the images. The appropriate scaling for the fringe correction was determined interactively.

Weak lensing applications demand precise measurements of the shapes of faint galaxies and therefore precise relative astrometric alignment of the individual dithered exposures of the field ($\sim 6''$ in our case). A transformation is needed between each chip of the input image and a common output grid which has to account for the position of the chip in the focal plane, rotation, variations in the height (and possibly an inclination) of the chip surface with respect to the focal plane, as well as any optical distortion induced by the telescope and camera optics. Fourth order polynomials were found to be sufficient to model these effects. The method that we have developed follows the approach described by Kaiser et al. (1999).

We use Digital Sky Survey (DSS²) images to define the external reference frame but then minimize the rms dispersion of the transformed object coordinates from all the exposures rather than the deviations between the transformed object coordinates from the corresponding DSS coordinates for each individual exposure. This approach ensures optimal *relative* alignment of the transformed exposures. The resulting rms dispersion of the transformed coordinates is of order $0''.01$, corresponding to $1/20$ of a CFH12k pixel, for usually $\gg 100$ objects per chip.

The input images are resampled onto the output grid with pixel size $0''.205$ (the median effective pixel scale of the CFH12k camera) using the software *SWarp* (Version 1.21). Pixel interpolation is done using the Lanczos3 kernel which preserves the signal well without introducing strong artifacts around image discontinuities (Bertin 2001). Fields with a large number of exposures (≥ 10) were averaged after rejecting outliers, those with fewer exposures median combined.

The images were photometrically calibrated on fields of standard stars taken from the list of Landolt (1992) with additional photometry by Stetson (2000). Atmospheric extinction was determined from sequences of science images spanning a sufficient range in airmass to allow accurate determination of the extinction coefficient.

2.2. Object detection

With the reduced and calibrated images in hand, the weak shear information must be extracted from the photometric catalogues. The analysis of the images involves a number of steps that we describe in detail below. These various steps are con-

¹ IRAF is distributed by the National Optical Astronomy Observatories, which are operated by the Association of Universities for Research in Astronomy, Inc., under cooperative agreement with the National Science Foundation.

² http://www-gsss.stsci.edu/dss/dss_home.htm,
<http://cadwww.dao.nrc.ca/dss/>

Table 1. Image detection parameters in the 3 filters B, R and I, and for the combined image called “C” (see Sect. 2.5 for details). We also indicate the number of detections in each image, their number density (expressed in arcmin^{-2} , in parenthesis), and the magnitude cuts for galaxies classification. Estimated average redshift \bar{z} and $\bar{\beta} = \langle D_{ls}/D_s \rangle$, with their standard deviations, are given for the faint galaxy catalogue (see Sect. 3.3 for details).

Filter	B		R		I		C (“Combined”)	
Date of observation	May 30/June 2 2000		May 30/June 2 2000		May 30/June 2 2000		-	
Number of exposures	4		5		5		-	
Exposure time (sec)	3600		3000		3000		-	
Seeing	0.91''		0.85''		0.88''		0.85''	
Completeness mag	24.9		24.3		22.6		24.4 (arbitrary 0-point)	
PSF anisotropy	0.032 ± 0.012		0.071 ± 0.019		0.064 ± 0.028		0.059 ± 0.023	
Number of Detections	34669	(28.6)	41067	(33.9)	28805	(23.7)	49977	(41.0)
Stars	2223	(1.8)	3488	(2.9)	2397	(2.0)	3692	(3.0)
Galaxies	25823	(21.3)	30189	(24.9)	21145	(17.4)	36711	(30.1)
Others	6623	(5.5)	7390	(6.1)	5263	(4.3)	9574	(7.9)
Bright galaxies	B<22.0	1171 (1.0)	R<21.1	2166 (1.8)	I<19.3	950 (0.8)	C<20.9	1941 (1.6)
Faint galaxies	22.5<B<25.4	20186 (16.7)	21.6<R<24.7	22794 (18.8)	19.8<I<23.3	14382 (11.8)	21.4<C<24.9	25174 (20.7)
Other galaxies	22.0<B<22.5		21.1<R<21.6		19.3<I<19.8		20.9<C<21.4	
	or B>25.4	4466 (3.7)	or R>24.7	5229 (4.3)	or I>23.3	5813 (4.8)	or C>24.9	9596 (7.9)
Faint galaxies \bar{z}	1.02 ± 0.42		1.06 ± 0.42		0.82 ± 0.35		1.04 ± 0.41	
Faint galaxies $\bar{\beta}$	0.70 ± 0.08		0.69 ± 0.08		0.65 ± 0.07		0.70 ± 0.08	

trolled in an (as much as possible) automatic way using different PERL scripts which allow a simple and easy handling of catalogues and can easily call external programme.

In the present paper we first treat the images taken in the three filters B, R and I *independently*. Differences between the results obtained from the three datasets are expected due to a number of effects. Different seeing of the images affects the accuracy of the measurement of galaxy shapes and hence the accuracy of the derived shear fields. Different photometric depths of the images will change the number density of faint background galaxies and thus again the accuracy of the shear measurements. Finally, the images sample different wavebands of the observed galaxies, which has an effect on the contrast between cluster and background galaxies if these are selected based on magnitude alone. This independent approach allows us to assess the uncertainties introduced by the mentioned effects. Of course it is desirable to eventually combine the information present in the three images in an optimal way so as to arrive at definitive measurements of the physical properties of the cluster. A first attempt at this combination is implemented here but will be discussed in more detail in a forthcoming paper.

The first step is to construct a master photometric catalogue of each individual image. For this purpose and to automatise the procedure as much as possible we have used SExtractor (Bertin & Arnouts 1996) in a 2 pass strategy. A first run is made to detect bright objects, with a detection level of 5σ above the background. The average size (full width at half maximum, FWHM) of the point spread function (PSF) is then easily determined from the sizes of stars. The saturation level of the image is also determined in this run. These parameters are then fed into a second SExtractor run with a lower detection level (1.5σ with a minimum size of 5 connected pixels above threshold). This second output catalogue corresponds to the working catalogue. The total number of objects detected in each image is given in Table 1. The photometry was computed using the MAG_AUTO method of SExtractor.

2.3. Star catalogue

The second step is to extract a star catalogue from the full catalogue which will then be used to estimate the local PSF. We select stars by a number of criteria. First we locate objects in the magnitude – μ_{\max} diagram (Fig. 2a) where μ_{\max} is the central surface brightness of the objects. Stars, for a given flux, have the highest peaked surface brightness (provided they do not saturate the CCD). Hence they populate the “star”-region of Fig. 2a, limited to a maximum value of the peak surface brightness by the saturation of the detector, and to a lower value, where galaxies start to overlap the star sequence.

We use an additional cut in FWHM indicated on Fig. 2b: objects with $\text{FWHM} > \text{seeing} + 1$ pixel are excluded from the star catalogue. Note that very compact objects (in the upper-right part of Fig. 2a) correspond to cosmic rays or noise defects in the overlapping region between chips. They are rejected and are put in the “other objects” catalogue (see Table 1).

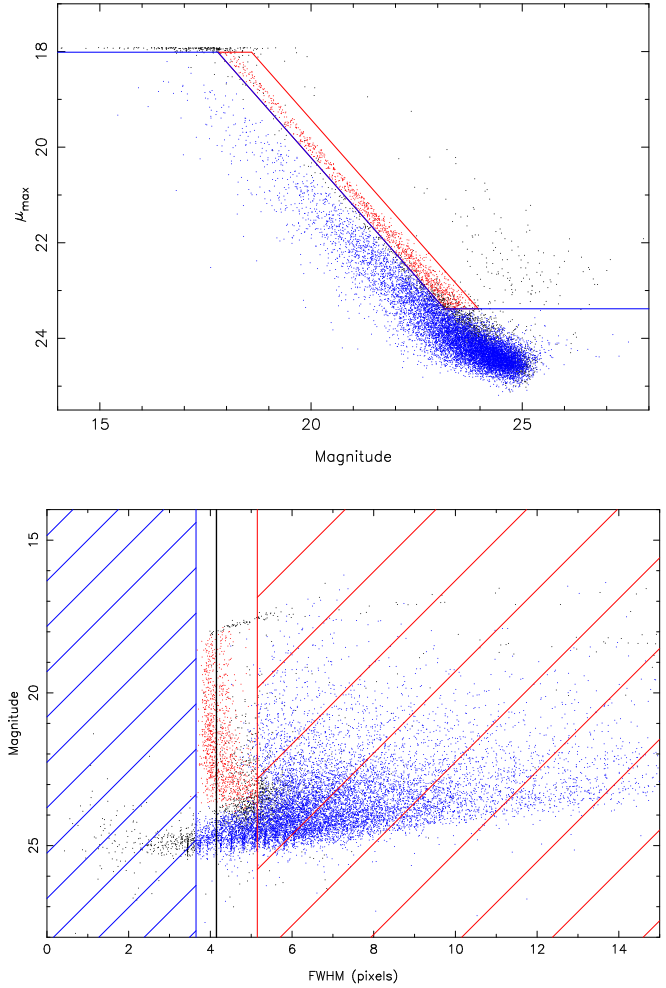


Fig. 2. Top: Magnitude- μ_{\max} diagram for all objects detected by SExtractor in the Abell 1689 R-band image. The points inside the parallelogram correspond to stars, the points below to galaxies. Points on the upper left correspond to cosmic rays, defects and saturated objects. Bottom: FWHM-magnitude diagram for all the objects detected by SExtractor in the Abell 1689 R-band image. The vertical black line indicates the average seeing value (4.15 pixels for the Abell 1689 R-band image). Stars are excluded from the right hatched part of the diagram ($> \text{seeing} + 1$ pixel), and galaxies from the left hatched part ($< \text{seeing} - 0.5$).

Finally, the star catalogue will be cleaned one last time (see Sect. 3.1) once the star shape will be adequately measured by IM2SHAPE.

2.4. Galaxy catalogues

The third step is to compute the galaxy catalogues that will be used to identify the faint lensed galaxies and the bright galaxies that are likely to be part of the cluster and which will be used to calculate the cluster luminosity.

Galaxies are selected from the Magnitude- μ_{\max} diagram (see Fig. 2a). First, as for the stars, saturated galaxies are excluded. We checked that none of the brightest galaxies in the

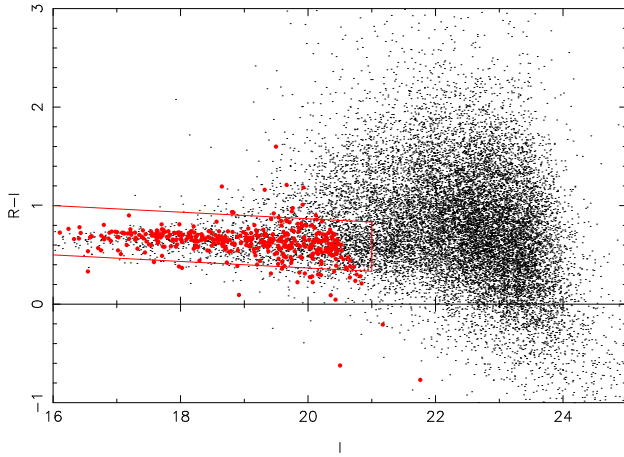


Fig. 3. Color-magnitude diagram for the galaxies detected in R and I filters. Bigger (red) points are the *R* bright galaxies (as defined in Sect. 2.4) closer than 300'' from the cluster center.

cluster core are affected by this cut which only affects lower redshift galaxies. Furthermore, we applied two additional cuts: galaxies must have a `SETRACTOR CLASS_STAR` parameter lower than 0.8 (this removes faint stars or faint compact galaxies from the catalogue), and galaxies cannot be smaller than stars, so we exclude all objects with a FWHM smaller than seeing-0.5 pixel. This blind cleaning is done in a similar way in all three bands as well as in the combined frame (see Sect. 2.5). These cuts remove most of the defects in the catalogues.

The galaxy catalogue is then split into 3 subcatalogues, defined by their magnitude range: one for the brightest galaxies, dominated by the cluster members, one for the faintest galaxies expected to be background sources, and the last one for the remaining galaxies (intermediate magnitude range galaxies or excluded objects).

The brightest galaxies catalogue is defined with respect to the apparent m^* of cluster galaxies (see Sect. 6.2 for the estimate of m^* in each filter). In order to keep a good contrast between cluster galaxies and the background field population but still integrating a fair fraction of the luminosity function, we define the bright galaxy catalogue by selecting galaxies down to $m^* + 2$ for the B and I-band and $m^* + 3$ for the R-band. We choose these limits in order to maximise the population of cluster members but still keeping a substantial number of background galaxies. The deeper R-band image allows to have fainter cuts. For Abell 1689, this corresponds to the magnitude limits $B < 22.0$, $R < 21.1$ and $I < 19.3$. This “bright galaxy” catalogue is considered in the rest of the paper as a likely “cluster catalogue” for which we can measure the cluster luminosity, derive a light map and which allows simple comparisons from one cluster to another.

Fig. 3 shows the color ($R - I$) - magnitude (I) diagram for the galaxies matched in both R and I filters (see Sect. 2.5). The *red sequence* of cluster ellipticals is well defined. The *bright galaxies*, as defined above, are plotted in big red points. They mainly follow the elliptical red sequence, which indicates that their identification with cluster members is largely correct.

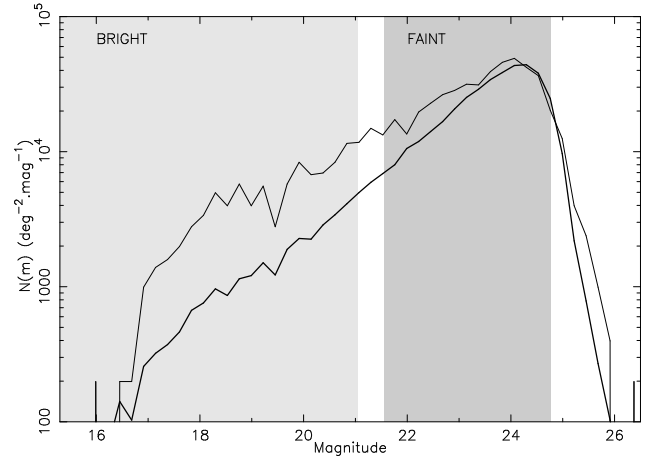


Fig. 4. Number counts of galaxies in the Abell 1689 R-band image in bins of 0.23 magnitude. The thick line corresponds to the galaxies across the whole field, the thin line to galaxies within 300'' from the cluster center. The grayed area to the left (respectively to the right) shows the magnitude selection for bright galaxies (respectively for the faint galaxies).

A second catalogue is created for the faint galaxies, with the following limits: $m^* + 2.5 < m < m^c + 0.5$ for the B and I-band catalogue and $m^* + 3.5 < m < m^c + 0.5$ for the R-band catalogue (m^c is the completeness magnitude which varies from filter to filter, see Table 1). These catalogues are dominated by faint and distant galaxies and are therefore considered as catalogues of background galaxies lensed by the cluster. The different cuts were adjusted in order to separate the bright (foreground) and faint (background) galaxies as much as possible without losing too many galaxies (see Fig. 4).

2.5. Combined image and cross-matched catalogue

As gravitational lensing has no wavelength dependence, we also produce a combined image from the 3 broad-band images. The input images have roughly the same properties in terms of exposure time, seeing, and PSF anisotropy (see Table 1), so we adjust the backgrounds to a common level before the combination, and rescale the images to a similar sky noise level to then optimally combine the flux of each filter. The sum of these 3 rescaled images is the combined “C” image the properties of which are listed in Table 1.

The combined image is deeper than each original image, so the total number of detections is largely increased. A cross-matching is then carried out by absolute position between the 4 sets of all *galaxies*. The position tolerance is set to the mean PSF FWHM (0''.87). Out of the 36,711 galaxies identified in the combined catalogue, 5,977 galaxies correspond to new detections, and 11,912 galaxies are detected in all 4 catalogues (B, R, I and C).

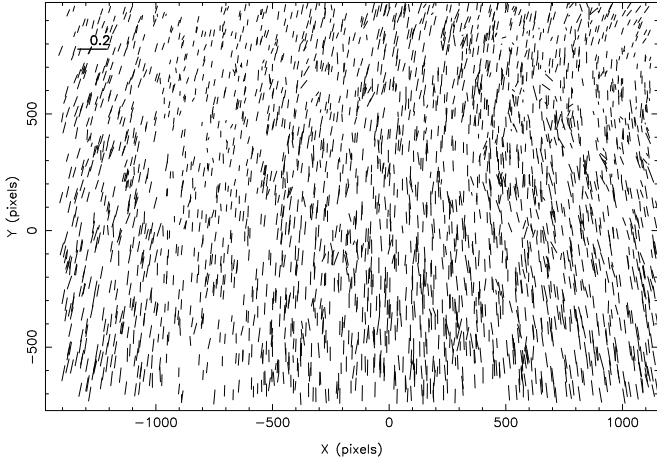


Fig. 5. Abell 1689 R-band PSF map. The length of the segments is proportionnal to ellipticity as indicated by the scale in the upper-left corner. Reference point (0,0) is the cluster center. See details in Sect. 3.1.

3. Galaxy shape measurements

Stars detected in the images are a good approximation of the point spread function (PSF) which measures the response of the entire optical system (atmosphere + telescope optics) to a point-source. The star shape is the result of the temporal integration over the exposure time. It includes an isotropic component mainly due to atmospheric seeing, as well as an anisotropic component caused for example by small irregularities in the telescope guiding. The isotropic component of the PSF leads to a circularization of the images of small galaxies and thus reduces the amplitude of shear measurements. The anisotropic PSF component introduces a systematic component in galaxy ellipticities and thus causes a spurious shear measurement if not corrected (Kaiser et al. 1995). The geometric distortions of the camera and the corresponding instrumental shear are corrected during the data-reduction procedure when the image is reconstructed on a linear tangential projection of the sky on a plane.

In the case of Abell 1689, which is well representative of the entire dataset, the mean anisotropy of the PSF expressed in terms of ellipticity $\epsilon = (a - b)/(a + b)$ is much smaller than 0.15 in each filter (see Fig. 5).

In order to correct for both the PSF circularisation and the PSF anisotropy, we use the Im2SHAPE software developed by Bridle et al. (2001). Im2SHAPE implements a Bayesian approach to measure the shape of astronomical objects by modeling them as the sum of elliptical gaussians, convolved by the local PSF which is also parametrized in terms of elliptical gaussians. The minimisation procedure of Im2SHAPE estimates the posterior probability distribution of the image given the model and the PSF, and Markov Chain Monte Carlo sampling gives the most probable value for each parameter, with the errors linked to the dispersion of the samples. This approach is a practical implementation of the idea presented by Kuijken (1999). Im2SHAPE is now becoming popular, and has been used in a number of weak

lensing applications using different instruments (Kneib et al. 2003; Cypriano et al. 2003; Faure et al. 2004).

A detailed comparison between Im2SHAPE and the KSB method is discussed by Bridle et al. (in prep.). In the following we describe in detail the procedure implemented to transform the catalogue data into source ellipticity parameters useful for a weak lensing inversion. For simplicity, only one elliptical gaussian is used to describe both the shape of the stars and the galaxies. Indeed, as shown in Fig. 6, star profiles are well fitted by a single gaussian. Furthermore, orientation and ellipticity (the most useful parameters for the weak lensing analysis) are relatively insensitive to the model used to describe luminosity profiles. The *a posteriori* justification of the validity of the choice is demonstrated by the quality of the weak lensing measurements.

3.1. Mapping the PSF distribution over the mosaic

In a first step, Im2SHAPE is used to measure the local PSF by estimating the shapes of all the stars in the star catalogue. The resulting PSF catalogue is then inspected in detail. We first remove objects with ellipticity greater than 0.2 which mainly appear to be defects between the chips. Another cleaning is done by removing stars too different from their neighbours: if they are 2σ away from the mean value of the local seeing, they are automatically rejected from the PSF catalogue. The final cleaned star distortion map is presented in Fig. 5.

3.2. Faint galaxy shapes

In a second step, we interpolate at each galaxy position the local PSF from the shapes of the 5 closest stars (Fig. 6). This number of stars is large enough to locally interpolate the PSF, whereas a much larger number would over-smooth the PSF characteristics. The efficiency of the PSF measurement and interpolation can be directly tested on the star catalogues. Fig. 7 shows the resulting distribution of the intrinsic sizes of stars after deconvolution with the local PSF. They are intrinsically much smaller than $1/10^{\text{th}}$ of a pixel.

Im2SHAPE then computes the intrinsic shapes of galaxies by convolving a galaxy model with the interpolated local PSF, and determine which one is the most likely by minimizing residuals. In the end, Im2SHAPE's output gives a most likely model for the fitted galaxy characterised by its position, size, ellipticity and orientation, and errors on all of these.

Fig. 8 shows how the galaxy ellipticity distribution is changed after the Im2SHAPE correction; the effect of PSF circularisation is evident.

3.3. Mean redshift of the faint galaxies

Although the photometric catalogues do not contain redshift information on the background sources, we attempt to estimate it statistically. Indeed, this is an ingredient of prime importance in the quantitative scaling of the mass distribution in a weak

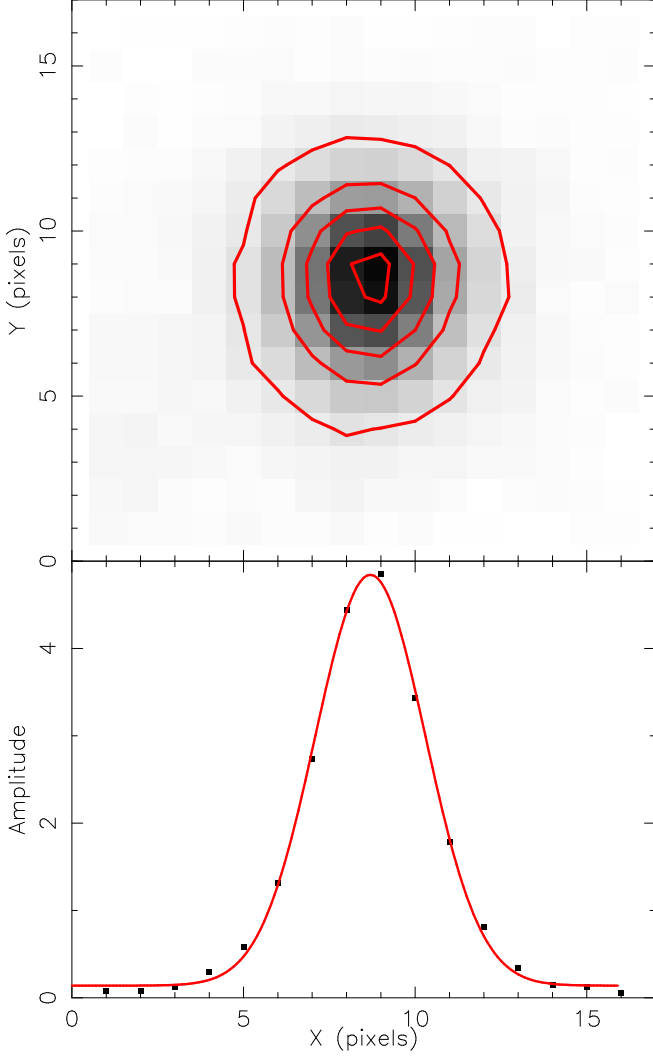


Fig. 6. Top: 16x16 image showing the superposition of the five (normalized) nearest stars of the (2000,2000) point (arbitrary position) in the R-band image of Abell 1689. Levels are from 0.5 to 4.5 in steps of 1. Bottom: A cut along the x -axis of the above image is indicated as small square and a gaussian profile fit (as done by Im2SHAPE) is indicated by a solid line.

lensing analysis. The important parameter in this application is the mean value of $\beta = D_{LS}/D_{OS}$:

$$\bar{\beta} = \frac{1}{N} \sum_{i=1}^N \frac{D_{LS,i}}{D_{OS,i}} \quad (1)$$

where N is the number of faint galaxies in the catalogue and D_{LS} is the angular diameter distance between the lens and the source and D_{OS} between the observer and the source.

One way to compute $\bar{\beta}$ is to assign a source redshift for each background galaxy. To achieve this, we have used a photometric catalogue produced from the *Hubble Deep Fields* (HDF) North and South, observed with the *Hubble Space Telescope* (HST) (Fernández-Soto et al. 1999; Vanzella et al. 2001). This catalogue, kindly provided to us by S. Arnouts (priv. comm.), contains for each object in the HDF the measured spectroscopic redshift if it exists (Vanzella et al. 2002) or a photometric red-

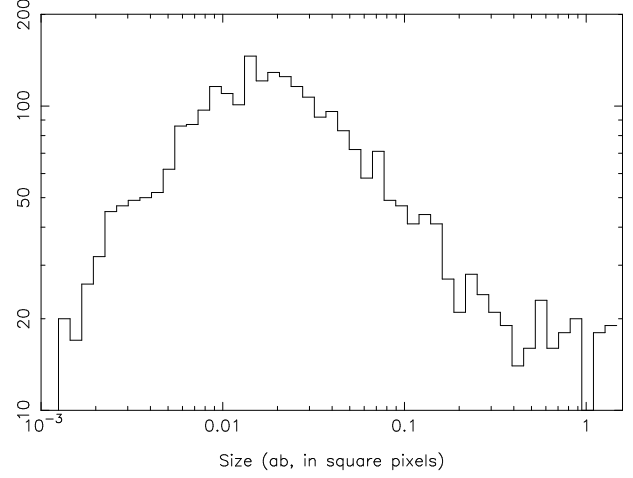


Fig. 7. Left: Size distribution ($a \times b$) of the deconvolved stars. Their size is much less than one pixel so we obtain the initial point-source.

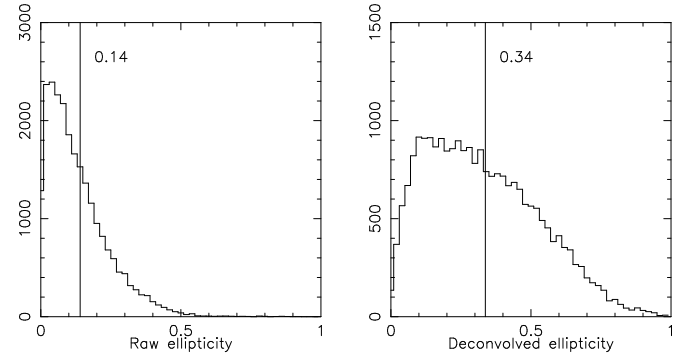


Fig. 8. Ellipticity distribution of the faint galaxies in the R-band image of Abell 1689. Left: Im2SHAPE catalogue with no PSF correction. Right: Im2SHAPE catalogue with PSF correction. The vertical line indicates the average value of the ellipticity. The effect of circularisation on the faint galaxies can easily be visualised by comparing both plots.

shift otherwise. Each galaxy detected in at least one of our three CFH12k images (B, R or I) has at least one entry in the corresponding photometric catalogues. Depending on the number of available magnitudes for each galaxy (1, 2 or 3) an automatic search for the 10 most similar objects (in terms of magnitude and colors, correcting for the slight differences between the photometric systems of the CFH12k and WFPC2 cameras) in the full HDF catalogue is done. Then the average photometric redshift (or spectroscopic if available) of these 10 objects is assigned to the galaxy. When all three magnitudes are available the procedure is close to a photometric estimate, while it is a simple statistical average of photometric redshifts for a given magnitude otherwise. Finally the mean redshift of each catalogue is computed, as well as the mean $\bar{\beta}$. Their values are given in Table 1.

4. Shear measurements

We have now measured the “true” shapes of faint galaxies and estimated their mean redshift. The lensing equation for galaxy shapes can be written in the weak regime as

$$\epsilon_I = \frac{\epsilon_S + g}{1 + g^* \epsilon_S}, \quad (2)$$

where ϵ_I and ϵ_S are the complex ellipticities of the image and the source; $g = \gamma/(1 - \kappa)$ is the reduced shear; γ is the shear vector and κ is the convergence (e. g. Mellier 1999). Note that both γ and κ are proportional to the distance ratio β .

Assuming that the faint galaxy population lies at the computed mean redshift, and assuming that galaxies have a random orientation in the source plane, it is easy to realize that by locally averaging a number of ellipticities we have an unbiased estimate of the reduced shear, and this will allow us to put strong constraints on the mass distribution:

$$\langle \epsilon_I \rangle = \langle g \rangle \quad (3)$$

The bracket signs $\langle \rangle$ indicate the average of a quantity near a position. However, because of the random orientation of the galaxies in the source plane, the error in the shear measurements and thus on the reduced shear will depend on the number of galaxies averaged together:

$$\sigma_g = \frac{\sigma_{\epsilon_S}}{2\sqrt{N}} \quad (4)$$

$\sigma_{\epsilon_S} \sim 0.33$ (see Fig. 8) is the dispersion of the intrinsic ellipticity distribution, and N is the number of galaxies used in the averaged.

We will explore different ways to do this averaging and constrain the cluster mass distribution.

4.1. Building the 2D shear map

The first and simplest test is to compute the 2D shear maps. To compute the *shear maps* we average the galaxies in square cells using the lensing catalogue (PSF-corrected faint galaxy catalogue). The cell size is chosen so that each cell contains about 35 galaxies. At the magnitude depth of the catalogues (~ 20 galaxies per square arcminute) this number is achieved for cells of $80'' \times 80''$ typically. With these numbers, the measured mean ellipticity should be small (smaller than 0.03 from Eq. 4) and its orientation random in regions with no shear signal. Near mass peaks, we expect to see an ellipticity excess, tangentially aligned around the center of mass. Fig. 9 clearly shows the characteristic lensing signal around the cluster core detected using the R-band catalogue of Abell 1689. This signal is traced by the coherent alignment of the “averaged” galaxies is represented by segments whose length is proportional to the ellipticity and whose orientation follows the mean orientation of the galaxies in each cell. Similar shear maps are seen in the two other bands.

4.2. Reconstructing the 2D mass map

We use the LENSENT2 code (Marshall et al. 2002) to compute the 2D non-parametric mass map of the clusters. LENSENT2

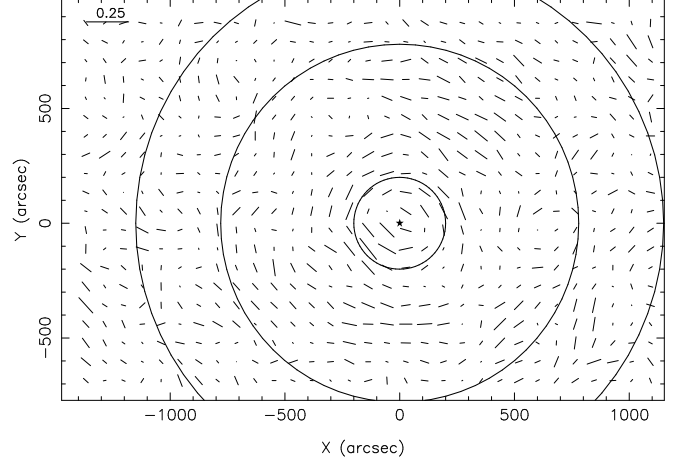


Fig. 9. Shear map for the R-band image of Abell 1689. The cluster center is marked by a “★”. The circles have radii of $200''$ (~ 620 kpc), $780''$ (~ 2.4 Mpc) and $1200''$ (~ 3.7 Mpc) respectively. The inner circle corresponds to the strong lensing region, the second one to the largest circle that lies entirely within the CFH12k image, and the outer circle marks the limit where the area outside the image becomes significant. The shear segments are computed in cells of $80'' \times 80''$, and have been smoothed by a gaussian of $30''$ width (see details in Sect. 4.1).

implements an entropy-regularised maximum-likelihood technique. It consists in a bayesian deconvolution process: a trial mass distribution $\Sigma(\theta)$ is used to generate a predicted (measured) reduced shear field through the convolution of the surface mass density by a kernel (KS93: Kaiser & Squires 1993). Contrary to KS93, LENSENT2 cannot produce negative feature in the mass maps. That’s why $\Sigma(\theta)$ is initially set to a positive background value, which will constrain the edge values of the reconstruction. Moreover, LENSENT2 has been improved to take into account not the mean shear field but each individual lensed galaxy with its redshift (if known). As clusters of galaxies have smooth and extended mass distributions, the values of Σ on the field are expected to be correlated through a kernel called the Intrinsic Correlation Function (ICF). For practical use, LENSENT2 needs to be given on input for each lensed galaxy its position, its elliptical shape parameters (with errors), and an estimate of its redshift (we use the mean redshift as explained in Sect. 3.3). There is basically only one free parameter in the procedure, the Intrinsic Correlation Function (ICF) which measures the correlation between mass clumps. We choose a gaussian ICF, and let its width vary. The ICF size is optimised so that the reconstructed mass map does not present too much insignificant small-scale fluctuations, although small ICFs best fit the mass peak of the cluster, while large ones best fit the wings of the extended profiles. This optimisation is performed by maximising the *evidence* value of each reconstruction, which is the probability to observe these data for a given ICF width. For more details on LENSENT2 see Marshall et al. (2002).

The main cluster mass clump is systematically detected by LENSENT2. The code estimates the central surface mass density

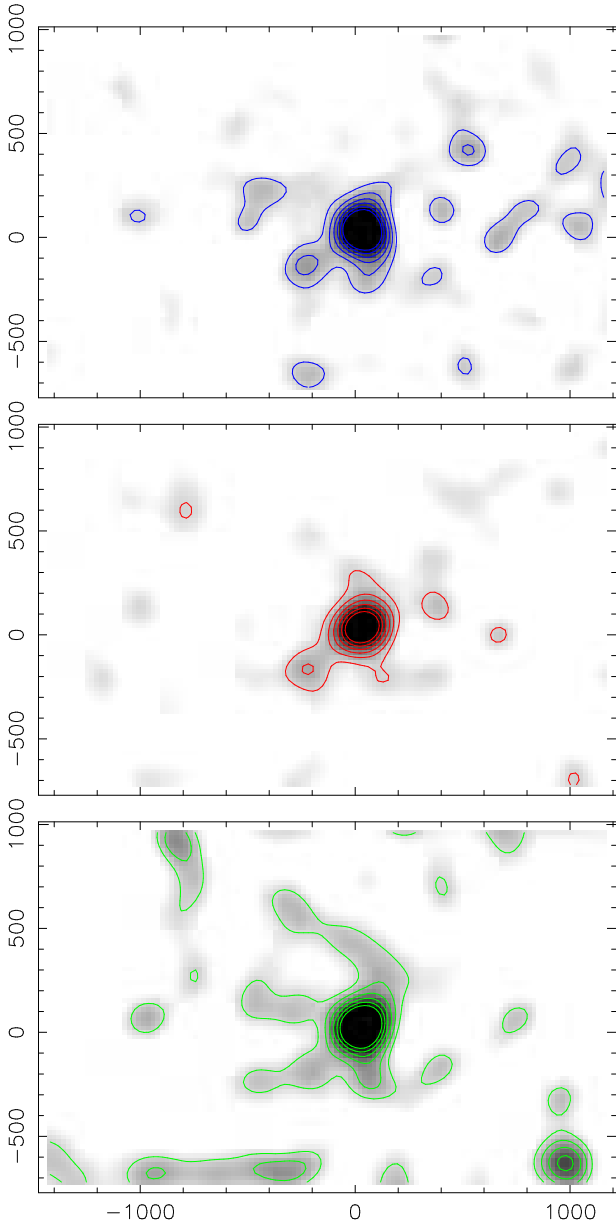


Fig. 10. LENS ENT2 mass reconstructions for Abell 1689 from the B (top), R (middle) and I (bottom) catalogues. The ICF is gaussian with a width of $180''$. The cluster peaks are at 1320 , 1250 and $1090 h_{70} M_{\odot} \text{pc}^{-2}$ for B, R and I respectively. White (black) in the gray scale is set to 1σ (5σ), and contours are at 2 , 3 , 4 and 5σ . σ values are estimated as explained in Sect. 4.2.

of the peak, and gives its spatial configuration. Note that large ICFs smooth the main peak. Reconstructions are computed for a large set of ICFs (from $60''$ to $240''$), and the best ICF width is found to be near $160''$ – $180''$ for our dataset. An illustrative example is shown in Fig. 1 or 10 where the peak of the surface mass density is at a value of $1250 h_{70} M_{\odot} \text{pc}^{-2}$ in the adopted cosmology, although typical values of the critical surface mass density for massive clusters at $z_L \sim 0.2$ are roughly around $\Sigma_c = 3200 h_{70} M_{\odot} \text{pc}^{-2}$ for sources at $z_S \sim 1.0$. This is because the ICF width used here ($180''$) is much larger than the typical value of the Einstein radius of the cluster ($\sim 40''$). Therefore

the smoothing process strongly attenuates the central peak density which in the case of Abell 1689 is clearly over-critical.

To assess the significance of the other mass density peaks detected in each image we modify the lensing catalogue by randomizing the orientation of the faint galaxies while position and ellipticity are conserved. We perform mass reconstructions of 200 randomized catalogues, and in each identify the 15 highest mass peaks. The statistics of these 3000 values gives a mean noise peak of $116 M_{\odot} \text{pc}^{-2}$ (99, 85) above the background level (set at $100 M_{\odot} \text{pc}^{-2}$ in input of LENS ENT2) in the R (B, I) image. This value is considered as the average fluctuation of the noise peaks, σ . With this definition, the cluster mass peak is detected at nearly 10σ above the background.

LENTS ENT2 mass reconstructions give many low significance mass peaks. For example, Fig. 10 shows that 4 clumps reach the 2σ level, but only one is above the 3σ level (main cluster excluded). To check their reality, we can compare the reconstructions in the three filters (B, R and I, Fig. 10). The regions where a mass clump is detected in the 3 images are considered as “real” ones and can be compared to the number density map of bright galaxies. Another test is to compare these clumps with any enhancement of the light distribution (Sect. 6.1), provided these mass clumps are not associated with “dark clumps”. The multi-color approach in this weak lensing study appears in this respect a powerful one to eliminate with high confidence most of the inconsistencies created in the mass reconstructions from some defects in the lensing catalogues. For Abell 1689, apart from the mass peak associated with the cluster, no other $> 3\sigma$ peaks were detected in all three filters. A possible 2 – 3σ peak is located $5'$ South-East of the cluster but no obvious optical counterpart in the galaxy distribution can be identified.

4.3. The radial shear profile

We have demonstrated that only one significant mass peak is detected in the Abell 1689 image, and that it corresponds to the massive cluster Abell 1689. In order to quantify the mass of this clump we focus the analysis on the radial distribution of the shear. Tangential and radial shears are computed as a function of the distance to the cluster center. They are averaged in annuli of width $\Delta R = R_2 - R_1$ for a mean radius $R = (R_1 + R_2)/2$. ΔR is kept constant so the S/N of the shear roughly decreases as $1/\sqrt{R}$, in order to keep enough independent points at large radii (a constant S/N requires too large annuli at those radii). A quasi-continuous profile is built by using a “sliding window” with steps Δr much smaller than ΔR . In practice, we chose $\Delta R = 160''$ (and $\Delta r = 10''$) for the Abell 1689 R image, so about 10 independent points are built in the profile.

Fig. 11 shows the tangential and radial shear profiles for the three images. The radial shear should be zero in the case of perfect data and a well chosen center for the annuli. In practice, it can be considered as an independent estimator of measurement errors (this is also referred to as the 45 degree test). In the case of Abell 1689, the radial shear is always lower than the tangential shear out to $\sim 1100''$, arguing for a good data quality in all 3 bands.

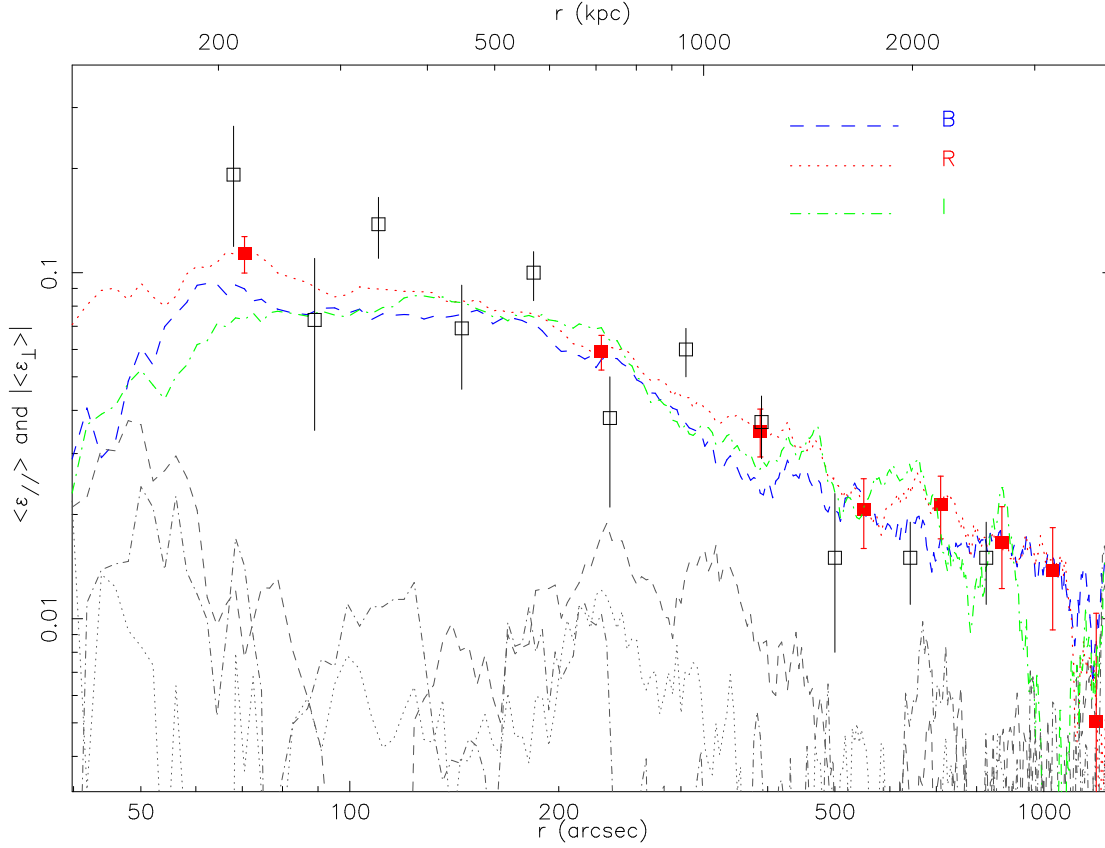


Fig. 11. Tangential shear profile for Abell 1689, in the B, R and I band. The bin width (ΔR) used here for the sliding window is $158''$. A series of uncorrelated points with error bars is displayed for the R band (solid squares). Absolute values of the associated radial component are indicated in grey, showing that the signal is well detected out to $\sim 1000''$ (3 Mpc) from the center. The measurements of Clowe & Schneider (2001) are also displayed for comparison (open squares).

Note that in the very center ($R < 70''$) the shear profile seems to drop. The error bars are large due to the low number statistics: the area considered is small, decreased by the masking effect of the bright galaxies. Moreover the depletion of the number density of background galaxies in the center due to the magnification bias (Taylor et al. 1998) also decreases the number of observable galaxies, although this effect is only important in the innermost annuli. This low number statistics does not completely explain the weakness of the shear: it can also be under-estimated if unlensed galaxies (such as cluster members) are included in the catalogues, which should be more likely towards the cluster core. As a consequence, the points inside $R = 70''$ will not be used in the modeling of the shear profile. The measurements done by Clowe & Schneider (2001) using R band images from the ESO Wide Field Imager (WFI) are also presented in Fig. 11 for comparison. Our measurements are quantitatively in good agreement with those of Clowe & Schneider (2001). Moreover, our error bars are smaller and our points less scattered, even if we consider the different binnings. This strongly suggests that the use of IM2SHAPE in the analysis process improves significantly the shear measurements. This will be quantified in a forthcoming paper (Bridle et al. 2004, in preparation).

5. Modelling the lensing data

5.1. Description of the mass models

Three families of mass models are used to fit the computed shear profile: a singular isothermal sphere profile (SIS), a power law profile (Pow) and finally the “universal” NFW profile (Navarro et al. 1997). In addition we implemented the Aperture Mass Densitometry method (AMD) to compute a *non-parametric* mass profile from the shear profile itself (Fahlman et al. 1994). We recall briefly the basic equations for the mass density (ρ), shear (γ) and convergence (κ) profiles for the three models.

5.1.1. The Singular Isothermal Sphere model

This is the simplest mass profile used in lensing inversion. It is essentially given by the following equations:

$$\rho(r) = \frac{\sigma^2}{2\pi G r^2} \quad (5)$$

$$\kappa(\theta) = \gamma(\theta) = \frac{\theta_E}{2\theta} \quad (6)$$

$$\theta_E = \frac{4\pi\sigma^2}{c^2} \frac{D_{LS}}{D_S} \quad (7)$$

where σ is the velocity dispersion of the mass particles in the cluster. Note that once the cluster center is fixed, this profile depends on one parameter only (θ_E or equivalently σ), so only one degree of freedom is available in the fits.

5.1.2. The Power Law model

The Power Law model is a generalisation of the SIS model, where the slope of the mass density profile is a free parameter (Schneider et al. 2000).

$$\gamma(\theta) = \frac{q}{2} \left(\frac{\theta}{\theta_E} \right)^{-q} \quad (8)$$

$$\kappa(\theta) = \frac{2-q}{2} \left(\frac{\theta}{\theta_E} \right)^{-q} \quad (9)$$

where q is the slope of the Power Law ($q = 1$ for the SIS model). Once the cluster center is fixed, this model presents 2 degrees of freedom.

5.1.3. The NFW profile

The NFW profile results from density profile fitting of numerical simulations of dark matter halos (Navarro et al. 1995, 1997). This profile is starting to become a popular model used in cluster weak lensing analysis (Kneib et al. 2003) as it also fits well the observed shear profile, which is a test of its validity for real clusters. The mass density profile can be expressed as

$$\rho(r) = \frac{\delta_c \rho_c}{(r/r_s)(1 + r/r_s)^2} \quad (10)$$

$$\text{where } \delta_c = \frac{200}{3} \frac{c^3}{\ln(1+c) + c/(1+c)} \quad (11)$$

$$\text{and } \rho_c = \frac{3H^2(z)}{8\pi G}. \quad (12)$$

r_s is the scale radius, $H(z)$ the Hubble parameter and $c = r_{200}/r_s$ the concentration parameter which relates the scale radius to the virial radius r_{200} . This density profile is shallower than the SIS near the center but steeper in the outer parts. Similarly as the power law model, once the center is fixed, it has two degrees of freedom: M_{200} for the normalisation of the mass and r_s for the scale radius, or equivalently r_{200} and c . The details of the analytic expressions for the shear and convergence of the NFW profile can be found in King et al. (2002).

5.2. Weak lensing fit

Each of the three models presented above is fitted to the data with a least square minimisation over the parameter space of the models. The χ^2 value calculated here is written as:

$$\chi^2 = \frac{1}{N-1} \sum_{k=1}^N \left(\frac{\epsilon_k^t - g_{\text{model}}(x_k)}{\sigma_k} \right)^2, \quad (13)$$

where N is the number of data bins, and σ_k is the error on the tangential ellipticity. It is computed in each bin as the mean error on the tangential ellipticity (ϵ^t), weighted by the number

N_k of galaxies in the bin used to do the measurement: $\sigma_k = \langle \sigma_{\epsilon^t} \rangle_k / \sqrt{N_k}$.

The data in the outer regions at $r > r_{\text{max}}$, where the annuli reach the borders of the images and start to be cut due to the finite image size, are excluded. In practice, only the area where tangential shear is greater than radial shear is included in the fits. Furthermore, as explained in Sect. 4.3, we also exclude the central part of the data. In the case of Abell 1689 (R band), this corresponds to the radius range from $r_{\text{min}} = 70''$ to $r_{\text{max}} = 1100''$.

Table 2 summarizes the results of the fits, and Fig. 12a displays the resulting best-fit models. The lower quality of the fit by the SIS profile is easy to understand as it depends on 1 parameter only, contrary to the other two which are represented by 2 parameters. Moreover, the value of the Einstein radius deduced from the fit is significantly lower than the one measured from strong lensing (which is estimated to be $\theta_E = 41''$). Note that Clowe & Schneider (2001) deduced with their weak lensing analysis a value for the Einstein radius similar to our estimate.

The fit with a power law is slightly better as the slope of the profile is fitted to be shallower than isothermal, but the Einstein radius is reduced by 25%. However, King et al. (2002) found similar results with an even lower Einstein radius.

The universal NFW profile is the model that best fits our shear profile. The concentration parameter (c) is slightly smaller than the values found by Clowe & Schneider (2001) and King et al. (2002), whereas the virial radius r_{200} is very similar. The derived Einstein radius is however quite small and thus this model is not a good fit of the central part of the cluster.

The mass profile of this cluster can probably not be easily explained by these simple fitting formulae, but may require a more complex profile, like the inclusion of the cluster galaxy halos and possibly a steeper central mass distribution.

Fig. 12b represents the projected mass profiles from the previous fits computed with the equation

$$M(r) = \pi r^2 \Sigma_c \bar{\kappa}(r) \quad (14)$$

where $\bar{\kappa}(r)$ is the mean dimensionless surface mass density inside radius r .

5.3. The Aperture Mass Densitometry method

Instead of fitting analytical formulae, we can directly integrate the measured reduced shear to determine the cluster mass profile. This direct method has been developed by Fahlman et al. (1994) and is called "Aperture Mass Densitometry" (AMD). The function $\zeta(r_1, r_2)$ is defined as the difference between the average convergences (or mean projected mass densities) inside the radius r_1 and within the annulus between r_1 and r_2 :

$$\zeta(r_1, r_2) = \bar{\kappa}(r < r_1) - \bar{\kappa}(r_1 < r < r_2) \quad (15)$$

$$= \frac{2}{1 - (r_1/r_2)^2} \int_{r_1}^{r_2} \frac{\gamma_t}{1 - \kappa(r)} d \ln r. \quad (16)$$

The reconstructed mass inside the radius $r < r_{\text{max}}$ is therefore

$$M_\zeta(r) = \pi r^2 \Sigma_c \zeta(r, r_{\text{max}}), \quad (17)$$

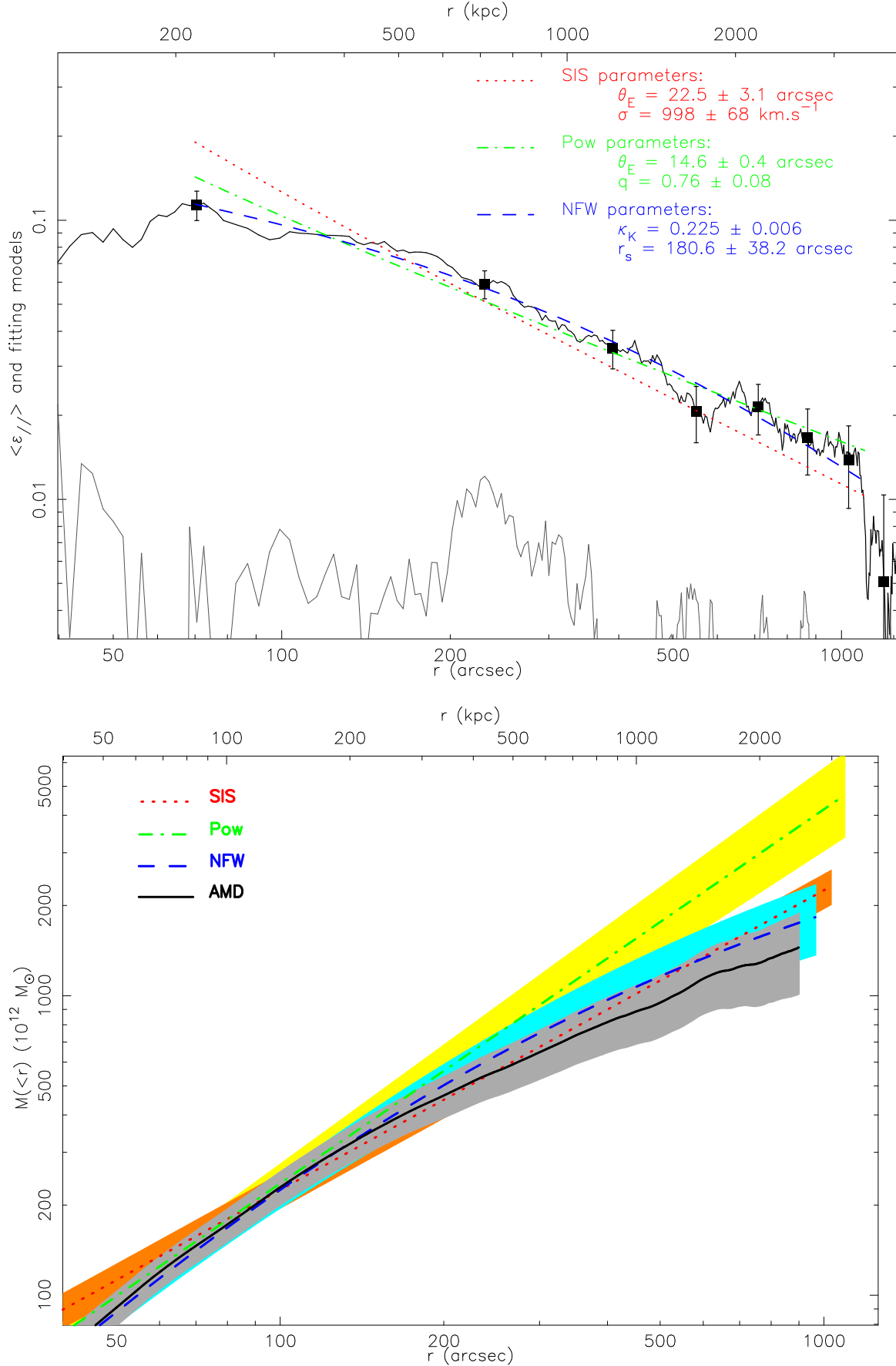


Fig. 12. Top: Best fitting parameters for SIS, Power law and NFW models, for Abell 1689 R-band shear profile. One series of uncorrelated points is shown (bin width = 158''). Bottom: Deduced mass profiles from these. The mass profile from the Aperture Mass Densitometry Method is also displayed, with a reference radius of 1100''. See text for details.

Table 2. Best fit results for the A1689 R-band shear profile. For the SIS, the results are given in terms of Einstein radius (θ_E) and velocity dispersion σ_{los} . For the Power Law, θ_E is again the Einstein radius and q the logarithmic slope. Finally for the universal NFW profile, c is the concentration parameter and r_{200} the virial radius. M_{200} is the projected mass inside r_{200} in units of $10^{12} h_{70}^{-1} M_{\odot}$ and θ_E is the derived Einstein Radius. (a) refers to the fit results from Clowe & Schneider (2001), (b) from King et al. (2002). The numbers in italic assume $z_s = 1.06$.

SIS	$\sigma_{1D} (\text{km s}^{-1})$	$\theta_E (")$	χ^2		
	998 ± 68	22.4 ± 3.0	1.98 (1)		
(a)	1028 ± 35	23.8 ± 1.6			
Pow	q	$\theta_E (")$	χ^2		
	0.75 ± 0.07	14.6 ± 0.3	0.637 (2)		
(b)	0.88	18.0			
NFW	c	$r_{200} (h_{70}^{-1} \text{ Mpc})$	$M_{200} (10^{12} M_{\odot})$	$\theta_E (")$	χ^2
	$3.5^{+0.5}_{-0.3}$	1.99 ± 0.25	1410^{+630}_{-470}	$2.6^{+1.4}_{-0.2}$	0.334 (2)
(a)	6.0	1.83	1030	9.7	
(b)	4.7	1.63	740	2.8	

where r_{max} is the maximum radius for which we can measure the shear or the radial limit of the data. In the case of our observations of Abell 1689, we choose $r_{\text{max}} \sim 1100''$, the maximum radius where annuli lie entirely within the field of view. Regarding Eq. 15, $M_{\zeta}(r)$ is only a lower limit to the *true* mass $M(r) = \pi r^2 \Sigma_c \bar{\kappa}(r)$ and should not be considered as an absolute mass determination.

The AMD mass profile is shown in Fig. 12 with the mass profiles derived by fitting analytical expressions. As expected, we find that the AMD mass is always smaller than the parametric mass estimates.

6. Light distribution and mass-to-light ratio

6.1. 2D light distribution

The catalogue of “bright” galaxies is assumed to be dominated by the galaxy cluster members, although it may also contain other bright galaxies within the field of view. Thus a density map (light density or number density) built from this catalogue can reveal other galaxy over-densities. In the case of Abell 1689, no over-densities other than the main cluster component are detected with high correlation with prominent peaks in the lensing mass distribution (Fig. 1).

We therefore focus on the light distribution assuming that the only over-density is due to cluster members. First in order to build a quantitative light density map or its radial profile, it is necessary to statistically correct the catalogue for the field contribution. Fortunately, the CFH12k images are large enough so that at a radius from the cluster center larger than $600''$ typically (2 Mpc at the cluster redshift) we assume that the outskirts of the cluster are reached and that the bright galaxy contribution is close to the “field” density. The mean number and light densities are therefore corrected by subtracting their minimal values estimated in the area $600'' < R < 1200''$.

Furthermore in order to estimate the total luminosity of the cluster and its radial profile, it is necessary to correct for the cut in magnitude in the catalogue corresponding to a cut in the cluster luminosity function (LF) and the incompleteness factor

C is estimated as follows. The cluster LF is assumed to follow the standard Schechter luminosity function (Schechter 1976):

$$\phi(L) = \frac{dN}{dL} = \frac{\phi^*}{L^*} \left(\frac{L}{L^*} \right)^{-\alpha} e^{-L/L^*} \quad (18)$$

Therefore the luminosity integrated in the catalogue down to a luminosity L_{inf} is

$$L_{\text{cat}} = \int_{L_{\text{inf}}}^{+\infty} L \phi(L) dL \quad (19)$$

$$= \phi^* L^* [\Gamma(2 - \alpha) - \Gamma(2 - \alpha, L_{\text{inf}}/L^*)] \quad (20)$$

so the fraction of the luminosity not taken into account when integrating within the magnitude limits of the catalogues is written as

$$C = \frac{\Gamma(2 - \alpha, L_{\text{inf}}/L^*)}{\Gamma(2 - \alpha)} \quad (21)$$

and the total luminosity is $L_{\text{tot}} = L_{\text{cat}}/(1 - C)$.

For the 3 bands used in this study, we need to estimate the 2 main parameters of the Schechter luminosity function α and L^* . These parameters depend on the choice of filters, on the galaxy type, and on the cosmological model. The best multi-color luminosity function determinations are presently those built from the Sloan Digital Sky Survey (SDSS) early release data (Blanton et al. 2001), although they correspond to field LF. The SDSS photometric system (u, g, r, i, z) is transformed to the CFH12k (Johnson) system by applying the transformations of Fukugita et al. (1996). In this paper we use the parameters of the LF summarized in de Lapparent (2003) and applied to a Sbc galaxy. Therefore the absolute magnitude M^* in the R filter is -21.83 in the adopted cosmology and the slope is $\alpha_R = 1.20$. This includes also the k-correction at redshift 0.18, computed with the galaxy evolutionary code by Bruzual & Charlot (2003).

Finally, the correction factors $1/(1 - C)$ are applied to L_{cat} to obtain the total integrated magnitude for the B, R and I catalogues, with the magnitude ranges defined in Sect. 2.4. The detailed numerical values are summarized in Table 3.

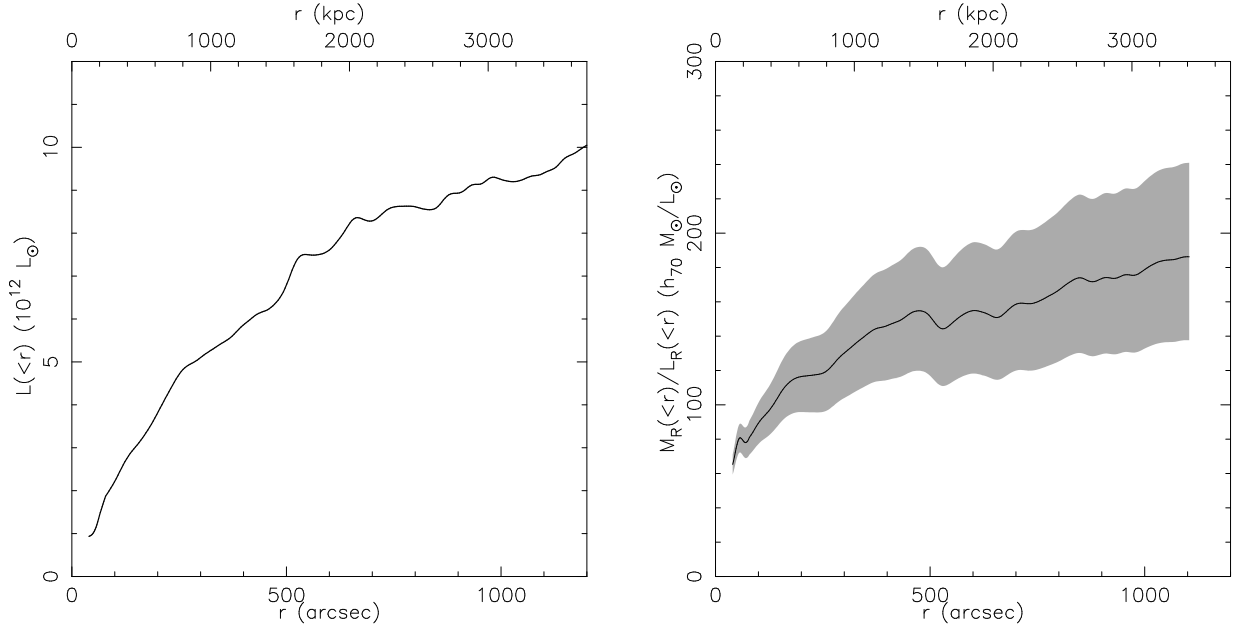


Fig. 13. Left: luminosity profile for the bright galaxy catalogue, for R band image of Abell 1689, corrected for background contamination. See Sect. 6.1 for details. Right: M_R/L_R ratio as a function of radial distance from cluster center, for Abell 1689, R image. The mass profile is estimated from NFW best fitted parameters. The filled region indicates the errors on the profile.

Table 3. Photometric parameters of the luminosity function in B, R and I filters for the adopted cosmology: $H_0 = 70 \text{ km s}^{-1} \text{ Mpc}^{-1}$, $\Omega_m = 0.3$ and $\Omega_\Lambda = 0.7$. The distance modulus is therefore $m - M = 39.70$ or equivalently the luminosity distance is $D_L = 872 \text{ Mpc}$, at $z_{\text{A1689}} = 0.18$. $1/(1 - C)$ is the correction factor applied to the integrated luminosity of the catalogues to get the total luminosity of the cluster.

	B	R	I
k-correction	1.06	0.16	0.16
$M^* - 5 \log h_{70}$	-20.47	-21.83	-21.54
α	1.30	1.20	1.25
$m^* (z = 0.18)$	20.29	18.03	17.32
$1/(1 - C)$	1.28	1.11	1.27

6.2. Comparison of mass and light: M/L radial profile

Using the NFW model (best fitting to the shear profile), the M/L profile is computed by dividing the luminosity profile, estimated from the bright galaxies catalogue, by the mass profile. The background component of this catalogue is estimated by measuring the minimum of the surface brightness density between $600''$ and $1200''$ from the cluster center. Fig. 13a displays this integrated luminosity profile for the R band image. Note that the L_R values were corrected using the correction factor discussed in the previous section.

Fig. 13b displays the $M_R(<r)/L_R(<r)$ profile with error bars estimated from the errors on the mass profile only. M/L starts from a low value (near $100 \pm 10 h_{70} (M/L)_\odot$ at 400 kpc from the center) and increases continuously to a flatter profile beyond $\sim 1 \text{ Mpc}$ at a value near $160 \pm 40 h_{70} (M/L)_\odot$. This behaviour is independent of the filter considered. It does however

depend slightly on the background subtraction at large radius, and on the detailed mass modelling in the inner part of the cluster. In particular, as we found a relatively small Einstein radius compared to the one observed from strong lensing, we might underestimate the mass in the central part, which would argue for an even flatter M/L profile towards the center.

Beyond $\sim 1 \text{ Mpc}$ the M/L ratio found in Abell 1689 is consistent with being constant with radius. This result is consistent with the findings of Kneib et al. (2003) in their lensing analysis of the cluster Cl0024+1654, both in the radial distribution and in the normalisation. For comparison, $(M/L)_R$ at large radii in the Coma cluster is found to be $170 \pm 50 (M/L)_\odot$ from dynamical analysis (Geller et al. 1999; Rines et al. 2001). Similar profiles for mass and light on 1–5 Mpc scales are expected if cluster assembly is largely governed by infalling groups and if no strong mass segregation occurs in the cluster depending on the nature of the mass.

In their sample of 12 distant clusters ($0.17 < z < 0.56$) Smail et al. (1997) found a mean value of $(M/L)_V^{\text{all}} = 126^{+147}_{-77} (M/L)_\odot$ ($h = 0.7$) in the cluster cores, where the superscript *all* refers to the entire population of the clusters, not only elliptical galaxies. Given the color index ($V - R$) of a mean Sa galaxy at redshift 0.19, this corresponds to $(M/L)_R^{\text{all}} = 102^{+119}_{-62} (M/L)_\odot$. Since our bright galaxies catalogue is dominated by elliptical galaxies (Fig.3), we expect to find a lower luminosity thus their M/L valeur is consistent with our findings.

7. Discussion and Conclusion

In this paper, we presented our methodology to analyze multi-color wide-field imaging data to constrain the mass distribution in clusters of galaxies using weak gravitational lensing.

The main scheme of the data analysis is the following: we use SExtractor for object detection and photometry and build several well-defined catalogues. The “stars” catalogue is used to determine the PSF locally, the “bright galaxies” catalogue is considered as dominated by cluster members and the “faint galaxies” catalogue mostly comprises background galaxies. The magnitude limits of each catalogue are determined with respect to the observational constraints such as the limiting magnitudes of the available images as well as physical constraints related to the magnitude distribution in the clusters at a given redshift. In order to determine the “true” PSF-deconvolved shape properties of the background (lensed) galaxies we use IM2SHAPE developed recently for the purpose of improving the quality of shear measurements, including a correct treatment of the measurement errors (Bridle et al. 2001). We then reconstruct the mass distribution by computing the shear profile and either fitting it with parametric mass models like the NFW mass profile or deducing the mass with the non-parametric Aperture Mass Densitometry method. Both methods are found to be consistent. We also propose a 2D mass reconstruction making use of the LENSENT2 software (Marshall et al. 2002) and applying it to the 3 images taken through the 3 filters. Finally we compute the M/L ratio as a function of radius, again in the 3 photometric bands. The 3 filters are used independently for most of the processing steps in order to confirm the significance of the results (comparison of shear profiles and mass maps). They give very consistent quantitative results, further demonstrating the robustness of our method. In complement, the images in the three filters are used jointly to estimate the background galaxies’ redshift distribution and to give a correct normalization of the mass determination.

We apply this method to the well-known cluster Abell 1689 as a test-case. We find only one significant mass peak in the mass reconstructions, corresponding to the cluster itself. This is consistent with preliminary results from a large spectroscopic survey of Abell 1689 and its outskirts (Czoske 2004), which shows that the environment of this cluster is remarkably smooth and quiet. We also compare our results to previous work by Clowe & Schneider (2001) who used an independent data set and the standard methods from Kaiser et al. (1995) and Kaiser & Squires (1993) for their galaxy shape measurements and mass reconstruction. Within the errors both reconstructions agree very well. The same is true for the M/L determination, which is consistent with previous findings. Moreover we are able to build a M/L profile which in the case of Abell 1689 shows a constant global trend at large radius with a possible decrease close to the centre. This suggests that mass traces light at least in the outskirts of the cluster. The drop of M/L in the cluster centre may be due to an underestimate of the mass in the centre, possibly because of increased contamination of the background galaxy catalogue by cluster members which dilute the lensing signal. The flat M/L profile in the infall region of the cluster indicates that the association between mass and light has already been achieved outside the cluster and the effect of the cluster environment on the mass-to-light ratio of infalling galaxies and groups is minor. This supports the picture of a hierarchical assembly of clusters.

For the results presented here we did not make use of the color information available from multi-band imaging to separate cluster from background galaxies which makes our results directly comparable to those of Clowe & Schneider (2001). However Clowe (2003) presented an updated mass reconstruction for Abell 1689, this time using colors derived from our CFH12k images. The color information resulted in an improved removal of cluster galaxies from his background galaxy catalogue, increasing both r_{200} and c for his best-fit NFW model and better agreement of the weak lensing mass profile with that derived from strong lensing. We will include color selection of the different galaxy catalogues in a forthcoming paper aimed at comparing in great detail all the mass estimates at different scales in Abell 1689: velocity distribution of the galaxies, X-ray mass maps, strong lensing in the centre of the cluster and weak lensing at larger scales. Provided the dynamics of the cluster is well understood this should give a consistent picture of its mass distribution and components. This is the main goal of the pan-chromatic survey which is conducted by our group on intermediate redshift X-ray clusters.

Finally, we will present a global study of our results based on the application of the present methodology to the whole cluster catalogue, with a discussion of the statistical properties of such clusters. A better understanding of the global properties of the mass distribution in rich clusters of galaxies provides a clue to the cosmological constraints related to the growth of structures in the Universe.

Acknowledgements. We wish to thank Sarah Bridle and Phil Marshall regarding the many interaction and helpful discussions we had, specially regarding IM2SHAPE and LENSENT2. We wish to thank CALMIP (CALcul en Midi-Pyrénées) for their data-processing resources during the last 2002 quarter, as the software used here is CPU-time and RAM consuming, and the Programme National de Cosmologie of the CNRS for financial support. JPK acknowledges support from CNRS and Caltech.

References

- Abell, G. O., Corwin, H. G., & Olowin, R. P. 1989, ApJS, 70, 1
- Andersson, K. E. & Madejski, G. M. 2004, astro-ph/0401604
- Bahcall, N. A., Fan, X., & Cen, R. 1997, ApJ, 485, L53+
- Bertin, E. 2001, SWarp v1.21 User’s Guide
- Bertin, E. & Arnouts, S. 1996, A&AS, 117, 393
- Blanton, M. R., Dalcanton, J., Eisenstein, D., et al. 2001, AJ, 121, 2358
- Bridle, S., Gull, S., Bardeau, S., & Kneib, J.-P. 2001, in Proceedings of the Yale Cosmology Workshop: “The Shapes of Galaxies and their Dark Halos”, ed. N. P. (World Scientific)
- Bruzual, G. & Charlot, S. 2003, MNRAS, 344, 1000
- Clowe, D. 2003, in ASP Conference Series, Vol. 301, Matter and Energy in Clusters of Galaxies, ed. S. Bowyer & C.-Y. Hwang, Chung-Li, Taiwan, April 23th-27th 2002, pp. 271–280
- Clowe, D. & Schneider, P. 2001, A&A, 379, 384
- Cuillandre, J.-C., Luppino, G. A., Starr, B. M., & Isani, S. 2000, in Proc. SPIE, Vol. 4008, Optical and IR

- Telescope Instrumentation and Detectors, ed. M. Iye & A. F. Moorwood, 1010–1021
- Cypriano, E. S., Sodré Jr., L., Kneib, J.-P., & Campusano, L. E. 2003, *astro-ph/0310009*
- Czoske, O. 2002, PhD thesis, Université Toulouse III – Paul Sabatier
- . 2004, *astro-ph/0403650*, to appear in *Proc. of IAU Colloq. 195: "Outskirts of Galaxy Clusters: Intense Life in the Suburbs"*, ed. A. Diaferio et al., Turin 12–16 March 2004
- Czoske, O., Kneib, J.-P., & Bardeau, S. 2003, in *ASP Conference Series, Vol. 301, Matter and Energy in Clusters of Galaxies*, ed. S. Bowyer & C.-Y. Hwang, Chung-Li, Taiwan, April 23th–27th 2002, pp. 281–290
- de Lapparent, V. 2003, *astro-ph/0307081*
- Ebeling, H., Edge, A. C., Allen, S. W., et al. 2000, *MNRAS*, 318, 333
- Ebeling, H., Edge, A. C., Bohringer, H., et al. 1998, *MNRAS*, 301, 881
- Ebeling, H., Voges, W., Bohringer, H., et al. 1996, *MNRAS*, 281, 799
- Eke, V. R., Cole, S., & Frenk, C. S. 1996, *MNRAS*, 282, 263
- Fahlman, G., Kaiser, N., Squires, G., & Woods, D. 1994, *ApJ*, 437, 56
- Faure, C., Alloin, D., Kneib, J.-P., & Courbin, F. 2004, *astro-ph/0405521*
- Fernández-Soto, A., Lanzetta, K. M., & Yahil, A. 1999, *ApJ*, 513, 34
- Fukugita, M., Ichikawa, T., Gunn, J. E., et al. 1996, *AJ*, 111, 1748
- Geller, M. J., Diaferio, A., & Kurtz, M. J. 1999, *ApJ*, 517, L23
- Girardi, M., Fadda, D., Escalera, E., et al. 1997, *ApJ*, 490, 56
- Kaiser, N. 2000, *ApJ*, 537, 555
- Kaiser, N. & Squires, G. 1993, *ApJ*, 404, 441
- Kaiser, N., Squires, G., & Broadhurst, T. 1995, *ApJ*, 449, 460, kSB
- Kaiser, N., Wilson, G., Luppino, G., & Dahle, H. 1999, *astro-ph/9907229*
- King, L., Clowe, D., & Schneider, P. 2002, *A&A*, 383, 118
- Kneib, J.-P., Hudelot, P., Ellis, R. S., et al. 2003, *ApJ*, 598, 804
- Kuijken, K. 1999, *A&A*, 352, 355
- Landolt, A. U. 1992, *AJ*, 104, 340
- Luppino, G. A. & Kaiser, N. 1997, *ApJ*, 475, 20
- Marshall, P. J., Hobson, M. P., Gull, S. F., & Bridle, S. L. 2002, *MNRAS*, 335, 1037
- Mellier, Y. 1999, *ARA&A*, 37, 127
- Navarro, J. F., Frenk, C. S., & White, S. D. M. 1995, *MNRAS*, 275, 720
- . 1997, *ApJ*, 490, 493
- Rhodes, J., Refregier, A., & Groth, E. J. 2000, *ApJ*, 536, 79
- Rines, K., Geller, M. J., Kurtz, M. J., et al. 2001, *ApJ*, 561, L41
- Schechter, P. 1976, *ApJ*, 203, 297
- Schneider, P. 1996, *MNRAS*, 283, 837
- Schneider, P., King, L., & Erben, T. 2000, *A&A*, 353, 41
- Smail, I., Ellis, R. S., Dressler, A., et al. 1997, *ApJ*, 479, 70
- Smith, G. P., Kneib, J.-P., Smail, I., et al. 2004, *astro-ph/0403588*
- Stetson, P. B. 2000, *PASP*, 112, 925
- Taylor, A. N., Dye, S., Broadhurst, T. J., Benitez, N., & van Kampen, E. 1998, *ApJ*, 501, 539
- Tyson, J. A. & Fischer, P. 1995, *ApJ*, 446, L55
- Tyson, J. A., Valdes, F., & Wenk, R. A. 1990, *ApJ*, 349, L1
- Valdes, F. 1998, *MSCRED V2.0: Guide to the NOAO Mosaic Data Handling Software*, available with the *mscred* software distribution
- Vanzella, E., Cristiani, S., Arnouts, S., et al. 2002, *A&A*, 396, 847
- Vanzella, E., Cristiani, S., Saracco, P., et al. 2001, *AJ*, 122, 2190
- Viana, P. T. P. & Liddle, A. R. 1998, *Ap&SS*, 261, 291
- Xue, S.-J. & Wu, X.-P. 2002, *ApJ*, 576, 152